Nanoscale

Accepted Manuscript

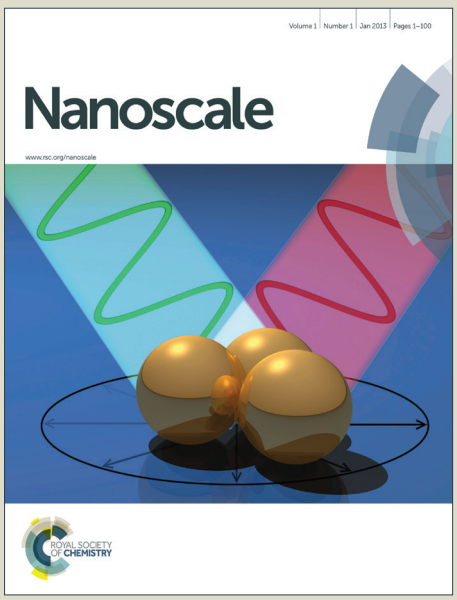

ROYAL SOCIETY OF CHEMISTRY

www.rsc.org/nanoscale

New insights into micro/nanoscale combined probes (nanoAuger, µXPS) to characterize Ag/Au@SiO_2 core-shell assemblies

J.B. Ledeuil*, A. Uhart, S. Soulé, J. Allouche, J.C. Dupin, H. Martinez

IPREM –ECP - UMR CNRS 5254, Université de Pau et des Pays de l'Adour, Technopole Hélioparc, 2 Avenue Président Pierre Angot, PAU Cedex 09,64053 Pau, France

***Corresponding author:** jean-bernard.ledeuil@univ-pau.fr*

ABSTRACT

This paper examines the elemental distribution and local morphology at the nanoscale of core@shell Ag/Au@SiO_2 particles. The characterization of such complex metal/insulator materials becomes more efficient using an initial cross-section method of preparation of the core@shell nanoparticles (ion milling cross polisher). The originality of this route of preparation allows one to obtain undamaged, well-defined, and planar layers of cross-cut nano-objects. Once combined with high resolved techniques of characterization (XPS, Auger and SEM), the process appears as a powerful way to minimize charging effects and to enhance the outcoming electron signal (potentially affected by the topography of material) during analysis. SEM experiments have unambiguously revealed the hollow-morphology of the metal core when Auger spectroscopy observations put into light a chemical heterogeneity within the particles (as silver and gold are randomly found in the core ring). To our knowledge, this is the first time that Auger nano probe spectroscopy has been used and successfully optimized for the study of some complex metal/inorganic interfaces at such a high degree of resolution (≈12 nm). In complement, XPS Au4f and Ag3d peaks were finally detected attesting of the possibility to access to the whole chemistry of such nanostructured assemblies.

Keywords: Core-shell nanoparticle, Ag/Au@SiO_2 , XPS, AES, Ion-milling cross section

1. Introduction

With the rise of nanoscience in recent decades, the design and development of advanced functional nanomaterials has undergone a large and rapid expansion due to their high potential in a wide range of applications such as electronics, energy storage, optics, catalysis, and nanomedicine [1–5]. In this context, multifunctional core-shell nanoparticles have emerged as attractive and promising nanoscaled entities, because they are able to combine several functions into a single unit. The multifunctionality can be provided by the combination of the different chemical natures and intrinsic properties of the core and parts of the shell. In addition, the design of nanostructured porous inorganic structures such as mesoporous silica, particularly in the shell, have been investigated to take advantage of their possible covalent anchorage by several functional organic molecules [6–8]. Such a design leads to so-called hybrid organic-inorganic materials characterized by novel or improved properties arising from a synergetic effect between the organic and mineral portions [4]. Among the variety of core-shell nanoparticle architectures encountered in the literature [9–13], the core noble metal-silica shell (NM@SiO_2) configuration has recently received much attention by researchers [14-20]. Our group recently demonstrated the possibility of coating Ag/Au nanoshells with an organically modified mesoporous SiO_2 shell to provide new photothermally responsive drug delivery nanomaterials [21,22]. The synthesis was performed through a sol-gel process that obtained well-defined and fine-tuned particles at the nanoscale. Nevertheless, given these dimensions in combination with the different chemical natures (silver, gold, silica, organic agents, etc.) of the core-shell zones, the control of the synergetic effect at the organic-inorganic and/or inorganic-inorganic interfaces becomes a key point in obtaining good and/or improved performance of the nanomaterials.

As a consequence, a better understanding of such particle-formation mechanisms at the nanoscale is required. Although it is challenging, it is now possible with the improvement of many analytical techniques, as recently demonstrated by Mattei *et al.* [23] for bimetallic core-shell nanospheres. Most micro-characterization techniques based on electron microscopy or spectroscopy must be alternately performed and the results compared to access the pertinent information about the considered nanosystems. For example, secondary electron microscopy (SEM) and transmission electron microscopy (TEM) are systematically and successfully used for metal core-SiO_2 shell morphological studies [24,25]. However, SEM is not sufficient to provide the core-shell chemical information when coupled with energy dispersion spectroscopy (EDS), because of the scale of the excitation volume. On the other hand, TEM

coupled with EDS or electron energy loss spectroscopy (EELS) is even more restricted, due to the possibility of sample preparation damage and analytical artifacts related to the thinning methods used for electron transparence and the utilization of a high primary beam energy [26–29].

In comparison, X-ray photoelectron spectroscopy (XPS) currently appears to be the most useful technique to get direct surfaces/interfaces information (chemical state, composition) for many research topics in advanced nanostructured materials [30,31]. The XPS sampling depth range varies from 1–8 nm depending on the particular analytical mode (e.g., angle resolved XPS; use of a higher energy than conventional Al-kα X-ray radiation).

In the case of core-shell structures, sometimes XPS analysis can be a powerful probe (even if it is not really considered to be a tool with "nano" resolution), given its potential to highly resolve chemical features [32,33]. However, if the analyzed core@shell particle size is larger than the material electrons escape depth (≈5nm) or if the inorganic shell is not porous enough, the relevant analysis becomes less effective due to core area signal attenuation. To overcome such limitations, and to record fine inner-particle chemical details, ion-milling cross section operations can be applied [34], which this work has taken advantage of in combination with a set of multiple high-resolution surface analytical techniques.

The cross-section preparation of samples has been possible for several years with dedicated techniques, some of which [35] require special skills associated with freeze fracturing, microtomy, or FIB methods. Other techniques [36] (e.g., mechanical polishing, cleavage, crushing, or electro-chemical polishing) are easily performed, but can induce sample damage.

Available since 2006, the ion milling method tends to be essential for preparing nanomaterials with regard to the efficiency of the polishing process [35,38]. The main technical difficulty is to perform a cross-cut section with a sufficient number of "polished" particles. Depending on the number of nanoparticles diluted in the matrix and the intersection of the cutting plane with them, the polishing process leads to cut spheres with random depths of cutting. To optimize the analysis conditions, the challenge was to define an appropriate "area of interest" in the cross-section layer for which the nanoparticles could ideally be well cut into half spheres. The cross-polisher method (CP) was then an original route to obtain a highly defined layer of cross-cut nanoparticles suitable for morphological and chemical surface analysis with μXPS, SEM, and SAM at the nanoscale. In particular, the extremely high spatial resolution of SAM (≈ 12 nm) was well-adapted for the challenging chemical and

morphological characterization of inorganic interfaces at the nanoscale. This constitutes a major key point, because the interface features are known to impact directly on a number of the properties of multicomponent based materials, especially core-shell nanoparticles. In addition to the overall description and discussion of the results to follow, we describe specific operational settings such as the excitation conditions, charging effect limitations, instrumental drift, and sample preparation techniques.

2. Materials and methods

2.1 Nanoparticles synthesis

Core-shell nanoparticles composed of an Au/Ag alloy core and a mesoporous silica shell (Ag/Au@SiO_2 nanoparticles) were synthesized following a procedure our group recently developed. The entire procedure and experimental details can be found in our recent publication [21]. Briefly, the synthesis is based on a two-step process whereby silver/gold alloy nanoshells were first elaborated by a galvanic replacement method using silver nanoparticles as patterns. In the second step, a surfactant-assisted sol-gel process was performed to coat the metal nanoshells with a well-defined mesoporous silica shell.

2.2. Preparation of nanoparticles for characterization

2.2.1 Non-cross-cut prepared particles

To prepare nanoparticles that were not cross-cut, the materials were simply deposited on aluminum foil before mounting on the sample holder for the XPS and SEM characterizations.

2.2.2 Cross-cut prepared particles: Ion-milling cross-section method

The cross-cut particles were prepared with a JEOL Cross-Polisher (JEOL Ltd, Tokyo, Japan). The particles were first diluted in a carbon paint (colloidal graphite) laid out on a 5 mm^2 Si wafer and then exposed to the Ar^+ ion beam (working pressure of 1×10^{-4} Pa; ion beam energy varying from 1 to 6 keV; ion current approximately 120 μA). The cross-cutting process is known to be precise and sharp, and it leads to a perfect planar surface as the beam angle to the sample surface is close to 90° (Fig. 1a). The shield plate blocks around 50% of the primary beam protecting the main part of the sample and then mainly allowing an edge

erosion of the material. Fig. 1b shows a wide SEM view of a Si wafer ultra-clean polished area (X, Y plane). Typical dimensions of the eroded area are 700 µm (X) × 400 µm (Y) × 40 µm (Z) obtained at 6 keV per 2 hours on the silicon wafer. In comparison with Ga^+ ions used in classical focused ion beam (FIB), the Ar^+ ion beam of CP process is achieved at low energy (1-6keV instead of 10-30 keV for FIB) and at grazing angle (typically 2° to the surface instead of 30-45 ° for FIB). Then it is less damaging for the specimen with extremely limited implantation of Ar^+ ions in the eroded surface [37](very low atomic mixing).

Figs. 1a and 1b

2.3 X-ray Photoelectron Spectroscopy (XPS)

XPS analyses were conducted with a Kratos Axis Ultra DLD spectrometer (Kratos Analytical Ltd, Manchester, UK) using focused monochromatized Al Kα radiation (hν = 1486.6 eV). The spectrometer was fitted with a double focusing 180° hemispherical analyzer (HSA) and a spherical mirror analyzer (SMA), which were run in fixed analyzer transmission mode (FAT) for the XPS data acquisition (FAT also known as constant analyzer energy mode CAE). The detector system is based on a delay-line detection used for both spectroscopy and 2-D imaging applications. The instrument work function was calibrated to produce a binding energy (BE) of 83.96 eV for the Au $4f_{7/2}$ line for metallic gold and a BE of 932.67 eV for the Cu $2p_{3/2}$ line for metal copper. The performance of the spectrometer on the Ag $3d_{5/2}$ photoemission line (BE 368.3 eV) was 250,000 counts at 0.48 eV full width at half maximum normalized to the full X-ray power. The coaxial Kratos patented charge neutralizer was used during the analysis to avoid any charge effect (i.e., coaxial electron flood gun working in accordance with a magnetic immersion lens) [39]. Survey spectra (wide energy range from -5.0 eV to 1200.0 eV BE) and parallel imaging were recorded at a constant pass energy (PE) of 160 eV (CAE mode) in high magnification lens mode for high sensitivity conditions at a power of 300 watts (20 mA/15 kV). Core ionization peaks were recorded at a constant PE of 80 eV (CAE mode) for the µXPS spectra and at 20 eV PE for the large area analysis (300–700 µm). Moreover, the µXPS analyses were achieved in the 15µm diameter selected small area XPS mode with the use of a selected area aperture inserted in the electrostatic lens column. Most XPS instruments are fitted only with optical microscopes suitable for macroscopic XPS analysis, which makes the ability to select small objects (<100µm)

difficult. Prior to running the μXPS analysis, SEM and high resolution XPS parallel imaging were both used to precisely define the position of the area of interest. For the high resolution parallel imaging using the SMA, the field of view was 200 × 200 μm with a spatial resolution of approximately 3 μm.

The spectra calibration was done by rescaling the experimental profiles based on the hydrocarbon contamination component of the C1s peak (285.0 eV). The peak fitting was processed with a nonlinear Shirley-type background [40], and the mathematical components were optimized with a weighted least-squares fitting method using 70% Gaussian and 30% Lorentzian line shapes. The quantification was performed with CasaXPS processing software (CasaXPS Ltd, Teignmouth, UK) using Kratos relative sensitivity factors [41,42]. The analysis chamber conditions were held constant under ultra-high vacuum (pressure<2.10^{-7} Pa). To prevent moisture or air exposure of the samples, the XPS spectrometer was directly connected to an argon dry box working at low H_2O/O_2 levels (<10 ppm through a fast load transfer chamber).

2.4 Auger Electron Spectroscopy (AES)/Scanning Auger microscopy (SAM)

The Auger analyses were carried out with a JEOL JAMP 9500F Auger spectrometer (JEOL Ltd, Tokyo, Japan) working under UHV conditions (pressure<2.10^{-7} Pa). The UHV equipment was a Schottky field emission Auger electron spectrometer (FE-AES) dedicated to very high spatial resolution analysis and high brightness. The hemi-spherical electron analyzer coupled with a multichannel detector (7 channeltrons) offered ideal settings for energy resolved Auger analysis.

Two modes were available for measuring the electron kinetic energy: constant analyzer energy (CAE) and constant retarding ratio (CRR). Classical AES experiments are usually recorded in the CRR mode, for which the energy resolution (dE) linearly increases with the measured electron energy (E) (the pass energy window varies to maintain a constant □E/E ratio). For comparison, the classical XPS analysis process runs with CAE with a constant energy resolution, regardless of the electron energy measured (dE/E variable). Technically, in CAE mode, the dE can be set at a value between 0.7 eV and 7.0 eV, corresponding to a fixed pass energy window between 10 eV and 500 eV. The spectra are provided in a direct mode N(E) (non-derivative mode expressed as the output signal of the electron detector using pulse counting versus kinetic energy). Qualitative "survey" AES spectra (kinetic energy from 0 to

2500 eV) were recorded using a focused probe and the CRR mode with a dE/E = 0.5% (high sensibility).

Scanning Auger line scans and images acquisition was performed in CAE mode to enable defining the useful energy width needed to obtain a significant peak background-intensity difference with respect to the Auger transition and the background shape. Different parameters such as the sample holder configuration (tilt angle), multi-detection conditions (number of Channeltrons on duty), acquisition time, and scanning rate (inducing the electron dose per point) were optimized.

A "soft etching" using low energy argon ion sputtering was applied to remove surface contamination on the samples prior to analysis. The etching parameters for the ion beam energy (500 eV), total ion current (0.1 μA), sputtering time (60s), and "compucentric" rotation [43] were carefully adjusted to avoid preferential sputtering, minimize induced sample roughness, and limit chemical damage.

An "auto probe tracking" correction was used to control and compensate for the drift, due primarily to the balance of the sample surface charge effects and the instrument-dependent fluctuations (e.g., vibrations, electronic and electromagnetic field variations, sample heat dissipation, etc.). The SAM and SEM images were recorded after each frame sequence and compared with an initial reference image to evaluate the total drift.

2.5 Scanning Electron Microscopy (SEM)

High resolution *high-energy* images were obtained with the previous JEOL JAMP-9500F Auger spectrometer (30 keV, 2nA, working distance = 23mm; same conditions than Auger spectroscopy analysis) fitted with a Schottky field emission electron gun using a conventional secondary electron detector (SED) in the analysis chamber. The present analysis mode permits a high depth of field for nanoparticles visualization.

High-resolution *low-energy* images were recorded with a JEOL JSM-7800F secondary electron microscope (2.5 keV, 0.5nA, working distance = 3mm). In these experimental conditions, the conventional SED minimizes the "backscattered" electrons coming out of the material and only gives an extreme surface visualization of nanoparticles. In addition, in the JEOL JSM-7800F secondary electron microscope, a second detector (in lens upper electron detector, UED) offers the possibility to collect "low energy-backscattered electrons" ("Z" contrast) [44–46].

3. Results and Discussion

3.1 Morphological and chemical analysis of non cross-cut Ag/Au@SiO_2 nanoparticles

3.1.1 SEM morphological analysis

After their synthesis, nanoparticles were characterized by SEM in order to control the expected core-shell hierarchical assembly. Particles appeared to be core-shell structured with a whole particle diameter of approximately 280 nm and a metal core size of around 100 nm (Fig. 2a). Indeed, same Fig. clearly highlights that under high primary beam energy conditions, two different material densities were observed: spherical shells and cores that appeared as "ghost" features in the central part of the assemblies. Fundamentally, with high primary beam energy, the SE contrast of the nanoparticles is composed of a direct shell surface signal (SE type1) and an indirect shell surface signal (SE type 2) induced by backscattered electrons interacting with the surface (Fig. 2b). Depending on the specific core-shell architecture, different density areas could then be observed in relation to the elements density (induced "Z contrast" SE image). Then, in the core@shell nanoparticles SEM image, the outermost shell appeared "transparent" because of the low density of the expected SiO_2 layer; particles of the second plane are even visible through this first low density zone. Moreover, the brilliant zone observed in the center would correspond to the expected high density metal core.

Figs. 2a and 2b

3.1.2 XPS chemical analysis

A classical XPS characterization was conducted to corroborate the previous SEM observations and to determine the chemical environments in the core-shell structure. Based on the high resolution core peak spectra shown in Fig.s 3a and 3b, the gold (Au4f) and silver (Ag3d) signals were not significantly detected. In contrast, the carbon, oxygen, and silicon (Si2p3/2-1/2 in Fig. 3c) peaks were recorded at BEs of 285.0 eV, 533.4 eV, and 103.6 & 104.2 eV, respectively, in agreement with carbon surface contamination (detected in all specimens: CC/CH bonds) and the SiO_2 environment of the shell. The quantitative O/Si ratio of approximately 1.4 was in good agreement with the common stoichiometry of unannealed silica [21].

In view of these results, although the silica shell was considered mesoporous structured [21], its thickness was definitively more than the XPS sampling depth (SEM showed a 90 nm thick SiO_2 layer around the 100 nm diameter Au/Ag core). Such XPS results point out the limitations of XPS spectroscopy for the analysis of these core-shell nanoparticles.

Fig. 3

3.2 Morphological and chemical analysis of cross-cut Ag/Au@SiO_2 nanoparticles

To go deeper in the fine description of the synthesized *Ag/Au@SiO_2* core@shell nanoparticles, some well-defined planar sections of undamaged individual nanoparticles were carried out. The preparation is supposed to reveal the inner core-shell structure and would allow the full characterization (elemental distribution and local arrangement) using combined and adapted techniques.

Fig. 4a displays a SEM large view of the cross-section area of in the carbon matrix (point 1) supported on a Si wafer (point 2). A close-up view of the central area (blue rectangle in Fig. 4a) is shown in Fig. 4b at a higher magnification. All the characterizations were conducted on the well-defined planar surface near point 3, as the present zone seems not to be affected by some charging effects (few nanoparticles diluted into carbon matrix) on the contrary of large aggregates near points 4 (high concentrated zone of nanoparticles with white SE contrast).

Figs. 4a and 4b

3.2.1 SEM morphological analysis

The images in Fig. 5 show an inclusion full of cross-cut nanoparticles (Fig. 5a) near the Si wafer plane, although only a few nanoparticles are ideally cross-cut in half-spheres (red arrows at the high magnification in Fig. 5b) due to their random distribution in the matrix. Fig. 6 illustrates the random cross-cutting of agglomerated nanoparticles. Those located partially above or below the ideal cutting-plane show a residual piece of sphere with an unsuitable view of the core structure. Giving preference to the half spheres makes morphological and chemical analyses of the whole core-shell structure possible.

Figs. 5a and 5b

The close-up morphological observations (Fig. 5b) reveal a spherical, hollow core-shell structure with a core ring approximately 20 nm wide and 100 nm in diameter. A noted benefit of the carbon matrix was the dilution of the charges within the whole material, thus reducing the charging effect inherent to the SiO_2 insulator.

Fig. 6

Finally, the cutting-plane offers a low surface roughness, reducing topographical shadowing effects and differential charging gradients that generally disturb photoelectron emission detection [31].

3.2.2 μXPS chemical characterization

The aim of next step of the study was to characterize by XPS, in the previous micro-domain of about 15μm diameter (see Fig. 5a), the inner chemical distribution of the aggregated cross-cut nanoparticles.

The main caution before running the μXPS analysis was to localize (coordinates X and Y) [47] the previous selected area with SEM. Fig. 7a displays the μXPS imaging issued from the overlay signals of carbon matrix (C1s peak (BE= 285.0eV, green)), silicon wafer (Si2p metal (BE= 99.0eV light red)) and nanoparticles (Si2p of silicon oxide shell (BE= 103.7eV, dark red)). The Fig. 7b presents the perfect matching between the SEM image and the XPS parallel imaging, permitting to locate the center of the "selected area". In this region, two inclusions of cross-cut core@shell nanoparticles are pinpointed by the marks "2" and "3" (Fig. 7c). The μXPS analysis was performed on the area "3" approximately 15 μm in diameter (same region previously analyzed with SEM, Fig. 5a).

Figs. 7a, 7b, and 7c

In contrast to the XPS data collected for the uncut nanoparticles (see §3.1.2, Fig. 3), all of the expected element transitions corresponding to several chemical environments were now

detected: silver metal (3d doublet at 368.6–374.5 eV; Fig. 8a), gold metal (4f doublet at 84.7–88.4 eV; Fig. 8b), the silicon of SiO_2 (2p doublet at 103.6–104.2 eV; Fig. 8c), and the oxygen of SiO_2 (532.9 eV). Other components related to the matrix and the surface contamination were also detected: the oxygen of the C-O-C bonds (534.6 eV), and the carbon of the C-C/C-H (285.0eV) and C-O-C (286.5eV) bonds (Table 1). In addition, the quantitative O/Si ratio [22.2% Si (Si2p) and 30.3% O from SiO_2 (O1s)] was approximately 1.4, in agreement with previous results obtained for uncut materials.

Figs. 8a, 8b, and 8c

Table 1

Even if the qualitative analysis of the inner nanoparticles was successfully done, the quantitative chemical overview is less evident and limited by the number of ideally cross-cut nanoparticles and the detection limit of μXPS (sensitivity). Some additional routes of characterization are then needed as the μXPS is not enough adapted for individual nanoparticle description even in the highest spatial resolution mode (3μm).

3.2.3 AES characterization

In this section, some first considerations are announced as the Auger analysis of non-conductive nanomaterials is rarely reported in the literature. Auger electron spectroscopy (AES) provides spatially resolved surface elemental information analysis and is complementary to the μXPS results [48,49]. Detected Auger electrons" are emitted from the first few surface nanometers, forming a volume of few nm^3 based on an area having approximately the size of the primary beam diameter and a depth resulting of Auger electrons escape depth (2-5nm for kinetic energy in the range of 20 eV to 2.5keV).

Consequently, the emitted signal does not suffer from the undesirable emission-volume effects generally observed with scanning electron microscopy coupled with X-ray emission spectroscopy. To adjust the Auger experimental settings for non-conductive nanomaterials, a preliminary step has consisted in: - finding the suitable operating conditions (excitations

conditions which give high sensibility with the minimum beam diameter), - drawing a strategy up to control the charging effect and the related drift parameter during the analysis. .

Several parameters of the excitation conditions could be optimized for the Auger signal to emerge from an intense background [50-52] more detailed in ESI:

- The energy beam (E_0) influences the ionization efficiency (σ) [53,54] and the background shape/intensity (BG), built up from the narrow secondary electron collection (0–50 eV KE range) and the wide backscattered electron collection (50 eV-E_0 range) (see Fig. ESI 1).

- The peak intensity (I^{Auger}) is directly connected to the relevant current for the highest sensitivity and a modulated probe diameter (Fig. -ESI 2).

Moreover, additional experimental cautions involved control of the charging effect of non-conductive samples and the possible instrumental drift over time, often noticeable for high magnification surveys. The electrical potential of the sample may be altered by the imbalance between the incoming and outgoing electrons, resulting in a surface charge build-up [55]. Indeed, two electronic flows, the primary electron (PE) injections in the specimen and the secondary electron emission, are in competition [56].

In the case of a non-conductive sample like the present Ag/Au@SiO_2 nanomaterials, the charge compensation mechanisms are drastically affected, generating a surface potential (Vs) that influences the energy, the direction of outgoing electrons, and the yield of secondary electron emissions (SE, BSE, and Auger). A self-regulation process then occurs to reach a steady state, with a residual Vs building up over time [57]. In general terms, to obtain a correct analysis, it was advisable to reduce the primary beam energy (excitation conditions optimization) and/or to use a defocused beam (increases the probed surface area, but loses spatial resolution) [58].

Classically effective methods that prevent a charging effect during AES experiments are primarily the charge neutralization [59], tilting [60], and sample thickness reduction methods [58]. In this work, we focused on the latter method, which is suitable for diminishing the number of surface residual charges (positive holes or primary electrons) that have diffused in the specimen. Our method using the cross polisher is consistent with the thickness reduction

strategy, as particles can be isolated (single or agglomerate) in a matrix and then cross-cut through the center. The area exposed to the electron beams or X-rays is then more strongly reduced than are the particles prepared without cross-cutting. The CP method also improves the electron transmission for a conductive sample holder (electronic dissipation) and the specimen heat dispersion.

3.2.3.1 AES characterization *of cross-cut Ag/Au@SiO_2 nanoparticles*

3.2.3.1.1 AES single point spectra

A quick AES survey was in a first time conducted on different points of the material to demonstrate the ability to chemically resolve the core and shell of the particles. Fig. 9 shows the high resolution SEM image (Fig. 9a) and AES spectra (red and black curves in Fig. 9b) of two characteristic points: the core (point 1) and shell (point 2) of a single cross-cut nanoparticle.

The analysis of point 1 showed unambiguously elements transitions for Ag_{MNN}, O_{KLL}, C_{KLL}, Au_{MNN}, and Si_{KLL} which attests of both the analysis of the metal core ring but even of the boundary of the SiO_2 shell. In contrast, only silicon, oxygen, and carbon were detected for point 2 as expected for the inorganic shell. For this set of analyses, the electron probe size was estimated at approximately 5nm during the applied excitation conditions (30.0 kV, 2nA), with a corresponding AES emission diameter of about 12 nm. These dimensions were compatible with the core-shell structure, and the recorded AES spectra confirmed the "spatially AES resolved analysis" on such nanostructured materials with clear electron transition signals.

Figs. 9- a) and b)

3.2.3.1.2 AES elemental mapping

Once the elements transitions detected, the second objective was to achieve a 2D elemental mapping of the observed species (Scanning Auger Mapping) to clearly overview the element distribution.

The RGB (Red Green Blue) synthesis (Auger relative intensity overlay) is displayed (Fig. 10 right) for any constitutive element in connection with the associated SEM image (Fig. 10

left). Results of an individual nanoparticle mapping have shown the core ring is clearly associated with silver (red) and gold (green), and the outermost shell is only made of silicon oxide (blue), as previously assumed.

Fig. 10

3.2.3.1.3 AES line profile experiments

An additional experiment was run in line scan mode to better understand the bimetallic alloy (fine elements spatial distribution at the nanoscale) and the metal/inorganic interfaces between the core and the shell. Line scan method offers the opportunity to significantly increase the signal to noise ratio (increase of the time per analyzed point) and to limit the irradiation damages onto the material as time of whole analysis is shorten than 2D mapping analysis.

Line profile experiments were performed continuously recording the AES peak intensity above the background along a straight line over the region of interest (Fig.11a). The probe displacement relative to this linescan is typically defined using a SEM image (bold horizontal white arrow in Fig. 11b). The AES signal-intensity variation corresponding to the previous main elements (Si_{KLL}, O_{KLL}, Au_{MNN}, and Ag_{MNN}) were recorded and then overlaid with the corresponding SEM image to gain a better understanding. The "experimental" Auger spatial resolution was evaluated in our conditions to be better than 12 nm (20-80% intensity variation)

The linescan analysis pointed out the following results:

- The Si and O intensity signals are mainly found across the outermost shell and vary in the same way while the Au and Ag signals are only detected in the core ring location as expected (see linescan from point 1to point 5, Fig.11b). Si signal is non-existent in the hollow region of the core@shell assembly (e.g., point 3, Fig.11b).
- Moreover, the Au and Ag intensity curves overlay together but in different proportions (see points 2 and 4 on Fig.11b) which confirms the non-homogeneous elemental distribution of metals in the core ring.

Figs. 11- a) and b)

In the hollow region of the nanoparticle (see point 3), the metals signals deeply decrease (but still existing) according to the half-sphere geometry (Fig. 12b). This evolution cannot be associated with a lack of metals in this zone as the high resolution low energy backscattered image (BSE) contrast of the same nanoparticle clearly demonstrated an intense emission coming from constitutive metals of the core ring (Ag , Au) confirming a nanoshell structure. This last information could not have been deduced from SEM image (Fig. 12a). On the basis of these considerations, one can better understand the 2D elemental maps (Fig.10 right) and the differences of brilliance due to geometrical effects (edge effects due to the oblique position of the analyzer relate to the cross-cut plane and the curved morphology of the core particle).

Figs. 12- a) and b)

This third Auger acquisition mode using a "line scan" appears very adapted to precisely describe a nanostructured assembly. Indeed, by continuously recording the small Auger intensity signal variation, one has then the capability to detect small concentration variation even smaller than the lateral resolution (given by the probe diameter d_0). It should then be noted the difference which exists between the ability to separate two nearby points (resolving power of imaging mode) and the smallest detectable detail (spectroscopic mode). The smallest detectable detail is related to the minimum detectable concentration x_m (correlated to the Auger peak, the background intensity and the acquisition time) [61].

4. Conclusion

This work described a deep and detailed morphological and chemical characterization of Ag/Au alloy@SiO_2 core-shell nanoparticles. For such "as-prepared" materials, it appeared difficult to extract some morphological information from electron microscopy survey (SEM). In the same time, it was not possible to access to the elemental distribution with the different high-resolution surface-analytical techniques (XPS, Auger). The aim of this work was then to propose a new route to reach the whole description of such core@shell assemblies. In this case, a set of different methods of characterization (SEM, μXPS, and AES) were combined with a specific cross-section preparation method using a cross polisher as an original and unique tool to reveal the inner structure of nanoparticles. The low energy SEM analyses

clearly demonstrated a hollow core structure. Moreover, depending on the random cross-cutting process, the images illustrated different "levels of cut," making it possible to reconstruct the inner geometry of the particles. The core and shell sizes could then be measured with a high accuracy. The whole core-shell nanoparticles had a circular shape, with a homogeneous diameter of 280 nm and consisted of a SiO_2 shell approximately 90 nm wide, hollow cores featuring a pseudo-circular shape with a diameter of about 100 nm, and a 20 nm homogeneous section.

The μXPS analysis on the small-cut clusters assembly compensated for the random distribution of the single-cut particles in the cross section. We then demonstrated the ability to characterize the core and the shell elemental composition (chemical state and content) at the same time. The binding energies of the XPS core peaks for Si2p, O1s, Ag3d, and Au4f were characteristic of silicon oxide for the shell and of an Au/Ag alloy for the core.

To improve the quantitative study of such core@shell assembly new routes could be investigated: improvement of the detection limit of the technique and/or higher concentration of nanoparticles in the cross section.

The original cross-section preparation method also appeared particularly well-adapted to Auger spectroscopy and mapping (AES, SAM) characterization due to the reduction of the surface roughness. Indeed, a well-defined surface with extremely low defects and good planarity induces a limitation on the geometrical effects and improves the electronic/heat dissipation in the matrix containing the nanoparticles. By optimizing the excitation conditions, very highly and spatially resolved Auger spectroscopy was performed successfully on a single cross-cut nanoparticle, with the line profile analyses correlated to the Auger mapping revealing the differences in gold and silver content between the innermost and outermost structure of the nanoparticle.

Finally, this is the first time to our knowledge that Auger spectroscopy has been used at such a level of resolution (≈12nm). Interestingly, these techniques open promising opportunities for a better understanding of solid-solid interface phenomena and are not limited to core-shell nanoparticles, but can also be used for numerous kinds of "composite" materials such as thin solid films.

Compared to the often damaging sample preparation methods inherent to conventional analytical techniques, including TEM, EDS, and EELS, the preparation technique utilizing a cross polisher allowed for an easier-to-handle procedure and non-damaging implementation,

which was associated with reduced roughness and a high degree of definition of the analyzed surface.

Acknowledgements

The authors wish to acknowledge JEOL Company Limited, and especially A. Tanaka and Y. Yamamoto, for their SEM, CP and AES support. We also thank P. Weisbecker from Laboratoire de Composites Thermostructuraux (Univ. of Bordeaux, Fra) for many discussions about cross-section preparation and TEM applications.

References

[1] N. Giuseppone, Toward self-constructing materials: a systems chemistry approach, Accounts Chem. Res. 45 (2012) 2178–2188.

[2] C. Liu, F. Li, L.-P. Ma, H.-M. Cheng, Advanced materials for energy storage, Adv. Mater. Weinh. Ger. 22 (2010) E28–E62.

[3] R. Hao, R. Xing, Z. Xu, Y. Hou, S. Gao, S. Sun, synthesis, functionalization, and biomedical applications of multifunctional magnetic nanoparticles, Adv. Mater. Weinh. Ger. 22 (2010) 2729–2742.

[4] C. Sanchez, B. Julian, P. Belleville, M. Popall, Applications of hybrid organic-inorganic nanocomposites, J. Mater. Chem. 15 (2005) 3559–3592.

[5] J. Jortner, C.N.R. Rao, Nanostructured advanced materials. Perspectives and directions, Pure Appl. Chem. 74 (2002) 1491–1506.

[6] P. Yang, S. Gai, J. Lin, Functionalized mesoporous silica materials for controlled drug delivery, Chem. Soc. Rev. 41 (2012) 3679–3698.

[7] T. Asefa, Z. Tao, Mesoporous silica and organosilica materials – Review of their synthesis and organic functionalization, Can. J. Chem. 90 (2012) 1015–1031.

[8] J. Allouche, A. Le Beulze, J.-C. Dupin, J.-B. Ledeuil, S. Blanc, D. Gonbeau, Hybrid spiropyran-silica nanoparticles with a core-shell structure: sol-gel synthesis and photochromic properties, J. Mater. Chem. 20 (2010) 9370–9378.

[9] H. Wang, L. Chen, Y. Feng, H. Chen, Exploiting core-shell synergy for nanosynthesis and mechanistic investigation, Accounts Chem. Res. 46 (2013) 1636–1646.

[10] X. Du, J. He, Spherical silica micro/nanomaterials with hierarchical structures: synthesis and applications, Nanoscale 3 (2011) 3984–4002.

[11] L. Wang, H.-Y. Park, S.I.-I. Lim, M.J. Schadt, D. Mott, J. Luo, X. Wang, C.-J. Zhong, Core@shell nanomaterials: gold-coated magnetic oxide nanoparticles, J. Mater. Chem. 18 (2008) 2629–2635.

[12] M. Sastry, A. Swami, S. Mandal, P.R. Selvakannan, New approaches to the synthesis of anisotropic, core-shell and hollow metal nanostructures, J. Mater. Chem. 15 (2005) 3161–3174.

[13] S.J. Hurst, E.K. Payne, L. Qin, C.A. Mirkin, Multisegmented one-dimensional nanorods prepared by hard-template synthetic methods, Angew. Chem. Int. Edit. 45 (2006) 2672–2692.

[14] A. Guerrero-Martínez, J. Pérez-Juste, L.M. Liz-Marzán, Recent progress on silica coating of nanoparticles and related nanomaterials, Adv. Mater. 22 (2010) 1182–1195.

[15] B. Khlebtsov, E. Panfilova, V. Khanadeev, O. Bibikova, G. Terentyuk, A. Ivanov, V. Rumyantseva, I. Shilov, A. Ryabova, V, Loshchenov, N.G. Khlebtsov, Nanocomposites containing silica-coated gold-silver nanocages and Yb-2,4-dimethoxyhematoporphyrin: multifunctional capability of IR-luminescence detection, photosensitization, and photothermolysis, ACS Nano 5 (2011) 7077–7089.

[16] B.J. Jankiewicz, D. Jamiola, J. Choma, M. Jaroniec, Silica-metal core-shell nanostructures, Adv. Colloid Interfac. 170 (2012) 28–47.

[17] K.-J. Lin, L.-J. Chen, M.R. Prasad, C.-Y. Cheng, Core-shell synthesis of a novel, spherical, mesoporous silica/platinum nanocomposite: Pt/PVP@MCM-41, Adv. Mater. 16 (2004) 1845–1849.

[18] P.K. Jain, X. Huang, I.H. El-Sayed, M.A. El-Sayed, Review of some interesting surface plasmon resonance-enhanced properties of noble metal nanoparticles and their applications to biosystems, Plasmonics 2 (2007) 107–118.

[19] D. Bartczak, O.L. Muskens, T.M. Millar, T. Sanchez-Elsner, A.G. Kanaras, Laser-induced damage and recovery of plasmonically targeted human endothelial cells, Nano Lett. 11 (2011) 1358–1363.

[20] S. Oldenburg, R. Averitt, S. Westcott, N. Halas, Nanoengineering of optical resonances, Chem. Phys. Lett. 288 (1998) 243–247.

[21] S. Soulé, J. Allouche, J.-C. Dupin, H. Martinez, Design of Ag-Au nanoshell core/mesoporous oriented silica shell nanoparticles through a sol-gel surfactant templating method, Micropor. Mesopor. Mater. 171 (2013) 72–77.

[22] S. Soulé, J. Allouche, J.-C. Dupin, H. Martinez, Advanced functional core-shell metal Ag-Au nanoshell/mesoporous silica nanoparticles : synthesis and photothermal/drug delivery coupling, submitted. (2013).

[23] J.G. Mattei, F. Pelletier, D. Ciuculescu, P. Lecante, J.C. Dupin, N. Yaacoub, J. Allouche, J.M. Greneche, D. Gonbeau, C. Amiens, J. Casanove, Formation of bimetallic FeBi

nanostructured particles: investigation of a complex growth mechanism, J. Phys. Chem. C, 117 (2013) 1477–1484.

[24] S.H. Joo, J.Y. Park, C.-K. Tsung, Y. Yamada, P. Yang, G.A. Somorjai, Thermally stable Pt/mesoporous silica core-shell nanocatalysts for high-temperature reactions, Nat. Mater. 8 (2009) 126–131.

[25] Y. Lu, Y. Yin, Z.-Y. Li, Y. Xia, Synthesis and self-assembly of Au@SiO2 core-shell colloids, Nano Lett. 2 (2002) 785–788.

[26] D. Eyidi, O. Eibl, A simple, quick and reliable method for TEM cross-section preparation of ceramic oxide films on thin metal substrates, Micron 33 (2002) 499–505.

[27] H.-H. Jin, H.-D. Cho, S. Kwon, C. Shin, J. Kwon, Modified preparation technique of TEM sample for various TEM analyses of structural materials, Mater. Lett. 89 (2012) 133–136.

[28] N. Jiang, On the limitation of quantitative measurements using transmission electron microscopy, J. Non-Cryst. Solids 358 (2012) 119–123.

[29] N. Jiang, J.C.H. Spence, On the dose-rate threshold of beam damage in TEM, Ultramicroscopy 113 (2012) 77–82.

[30] F. Reniers, C. Tewell, New improvements in energy and spatial (x, y, z) resolution in AES and XPS applications, J. Electron Spectrosc. Relat. Phenom. 142 (2005) 1–25.

[31] C.J. Powell, A. Jablonski, Progress in quantitative surface analysis by x-ray photoelectron spectroscopy: current status and perspectives, J. Electron Spectrosc. Relat. Phenom. 178–179 (2010) 331–346.

[32] G. Hota, S.B. Idage, K.C. Khilar, Characterization of nano-sized CdS-Ag_2S core-shell nanoparticles using XPS technique, Colloid. Surf. A 293 (2007) 5–12.

[33] I. Lopez-Salido, D.C. Lim, Y.D. Kim, Ag nanoparticles on highly ordered pyrolytic graphite (HOPG) surfaces studied using STM and XPS, Surf. Sci. 588 (2005) 6–18.

[34] N. Erdman, R. Campbell, A. Asahina, Precise SEM cross section polishing via argon beam milling, JEOL application note, Microsc. Today 14(3) (2006) 22–25.

[35] R. Langford, Specimen preparation for electron microscopy, in: P. Worsforld, A. Townshend, C. Poole (Eds.), Encyclopedia of Analytical Science, second ed., volume 6, Elsevier Academic Press, Oxford, 2005, pp. 124–134.

[36] D.A. Lucca, L. Shao, C.J. Wetteland, A. Misra, M.J. Klopfstein, M. Nastasi, Subsurface damage in (100) ZnSe introduced by mechanical polishing, Nucl. Instrum. Methods Phys. Res. Sect. B 249 (2006) 907–910.

[37] K. Tsutsumi, Auger analysis of cross sections prepared by cross section polisher, (46) JEOL News 41 (2006) 46–53.

[38] K. Ogura, M. Kamidaira, S. Asahina, N. Erdman, New methods for cross-section sample preparation using broad argon ion beam, Microsc Microanal. 13S02 (2007) 1518–1519.

[39]J.E. Fulghum, Recent developments in high energy and spatial resolution analysis of polymers by XPS, J. Electron Spectrosc. Relat. Phenom. 100 (1999) 331–355.

[40] D.A. Shirley, High-resolution x-ray photoemission spectrum of the valence bands of gold, Phys. Rev. B 5 (1972) 4709–4714.

[41] N. Fairley, A. Carrick, The Casa Cookbook, Part 1, Acolyte Science, Knutsford, United Kingdom, 2005.

[42] J.H. Scofield, Hartree-Slater subshell photoionization cross-sections at 1254 and 1487 eV, J. Electron Spectrosc. Relat. Phenom. 8 (1976) 129–137.

[43] A. Zalar, S. Hofmann, Comparison of rotational depth profiling with AES and XPS, Appl. Surf. Sci. 68 (1993) 361–367.

[44] K. Kumagai, T. Sekiguchi, Sharing of secondary electrons by in-lens and out-lens detector in low-voltage scanning electron microscope equipped with immersion lens, Ultramicroscopy 109 (2009) 368–372.

[45] J. Liu, High-resolution and low-voltage FE-SEM imaging and microanalysis in materials characterization, Mater. Charact. 44 (2000) 353–363.

[46] D.C. Joy, C.S. Joy, Low voltage scanning electron microscopy, Micron 27 (1996) 247–263.

[47] U. Vohrer, C. Blomfield, S. Page, A. Roberts, Quantitative XPS imaging-new possibilities with the delay-line detector, Appl. Surf. Sci. 252 (2005) 61–65.

[48] C. Le Gressus, Spectroscopie Auger - Techniques de l'Ingénieur, Editions Techniques de l'ingénieur, Paris, p2620-,1978.

[49] C. Burggraf, B. Carrière, S. Goldsztaub, Spectrométrie des électrons Auger, Rev. Phys. Appl. 11 (1976) 13–21.

[50] K.D. Childs, B.A. Carlson, L.A. La Vanier, J.F.Moulder. D.F.Paul. W.F.Stickle, D.G.Watson, Handbook of Auger Electron Spectroscopy, third ed., Physical Electronics Inc., Eden Prairie, Minnesota, 1995.

[51] C. Le Gressus, J. Cazaux, Spectroscopie Auger - Principes et performances en sonde fixe, Tech. Ing. Anal. Caract. p2620v2-1 (2007).

[52] M.P. Seah, I.S. Gilmore, Quantitative AES. VI. Backscattering and backgrounds—an analysis of elemental systematics and corrections of absolute intensity, Surf. Interface Anal. 26 (1998) 723–735.

[53] J.Ruste, Microanalyse X par sonde électronique - Principe et instrumentation, Tech. Ing. Anal. Caract. p885v2-1 (2012).

[54] C.S. Campos, M.A.Z. Vasconcellos, J.C. Trincavelli, S. Segui, Analytical expression for K- and L-shell cross sections of neutral atoms near ionization threshold by electron impact, J. Phys. B-At. Mol. Opt. Phys. 40 (2007) 3835–3841.

[55] J. Cazaux, e-Induced secondary electron emission yield of insulators and charging effects, Nucl. Instrum. Methods Phys. Res. Sect. B. 244 (2006) 307–322.

[56] D.R. Baer, A.S. Lea, J.D. Geller, J.S. Hammond, L. Kover, C.J. Powell, M.P. Seah, M. Suzuki, J.F. Watts, J. Wolstenholme, Approaches to analyzing insulators with Auger electron spectroscopy: update and overview, J. Electron Spectrosc. Relat. Phenom. 176 (2010) 80–94.

[57] J. Cazaux, Secondary electron emission and charging mechanisms in Auger electron spectroscopy and related e-beam techniques, J. Electron Spectrosc. Relat. Phenom. 176 (2010) 58–79.

[58] J. Cazaux, Electron probe microanalysis of insulating materials: quantification problems and some possible solutions, X-Ray Spectrom. 25 (1996) 265–280.

[59] K. Tsustumi, T. Suzuki, Y. Nagasawa, Effective methods to prevent charging in Auger electron spectroscopy, JEOL News 36E (2001) 66–70.

[60] K. Tsustumi, Y. Nagasawa, T. Tazawa, Auger analyses using low angle incident electrons, JEOL News 42E (2007) 40–45.

[61] J. Cazaux, Detection limits in Auger electron spectroscopy, Surf. Sci. 140 (1984) 85–100.

Figs. Legends

Fig. 1. (a) Schematic view of the cross-section polishing process: the sample side not protected by the shield plate is polished with the Ar^+ ion beam; (b) SEM image of a Si wafer cross section obtained with the ion-milling polishing method (XY plan).

Fig. 2. (a) High energy (30 keV) SEM image of the non cross-cut Ag/Au@SiO_2 nanoparticles; (b) Schematic view of the "Z" core contrast origin for a single core-shell nanoparticle: secondary electrons induced by the primary beam (SE1) and secondary electrons induced by primary backscattered (SE2) electrons.

Fig. 3. XPS core peaks of non cross-cut Ag/Au@SiO_2 nanoparticles: (a) $Ag3d_{5/2\text{-}3/2}$; (b) $Au4f_{7/2\text{-}5/2}$; and (c) $Si2p_{3/2\text{-}1/2}$. On Fig. (b), 2σ and 3σ of background intensity level (BG) have been reported ($\sigma=\sqrt{BG}$, Poisson statistics, Rose Criterion for a confidence level of 95 %).

Fig. 4. Low (a) and high (b) magnification SEM images of the prepared cross-section sample with nanoparticles. Panel 4b is an enlarged view of the blue rectangle in panel 4a.

Fig. 5. Low (a) and high (b) magnification SEM images of a small inclusion of core-shell cross-cut prepared particles embedded in a carbon matrix. Panel 5b is an enlarged view of the red rectangle in panel 5a. Arrows point to nanoparticles ideally cross-cut in half spheres.

Fig. 6. Correspondence of schematic cross-cut view of nanoparticles and the low energy (2.5 keV) scanning electron microscopy image: relative particle positions to the cut plane correspond to different cross-cut diameters.

Fig. 7. (a) High resolution parallel XPS mapping of a cross-section; (b) Same HR XPS map overlaid onto the cross section SEM image; and (c) Panel 7c is an enlarged view of the red rectangle in panel 7b showing the small 15 μm inclusions of particles in the carbon matrix.

Fig. 8. μ-XPS spectra of cross-cut prepared particles: (a) $Ag3d_{5/2\text{-}3/2}$; (b) $Au4f_{7/2\text{-}5/2}$; and (c) $Si2p_{3/2\text{-}1/2}$.

Fig. 9. Analyzed point 1(red) and point 2 (black) of a cross-cut Ag/Au@SiO_2 nanoparticle: (a) high magnification SEM image; and (b) corresponding wide energy range AES spectra.

Fig. 10. High resolution Auger mapping (SAM) of a single cross-cut Ag/Au@SiO_2 nanoparticle (red dotted square in the left SEM image) - RGB synthesis from element SAM overlays (right): red (Au); green (Ag); blue (Si).

Fig. 11. AES "line scan" analysis of a cross-cut Ag/Au@SiO_2: (a) schematic view of the probe displacement during the line scan experiment; (b) AES elements line profiles overlaid with corresponding SEM image.

Fig. 12. Low energy (2.5 keV) SEM images: (a) SE image; and (b) BSE image of a cross-cut Ag/Au@SiO_2.

Table captions

Table 1

Micro X-ray photoelectron spectroscopy quantitative composition table of cross-cut Ag/Au@SiO_2 nanoparticles.

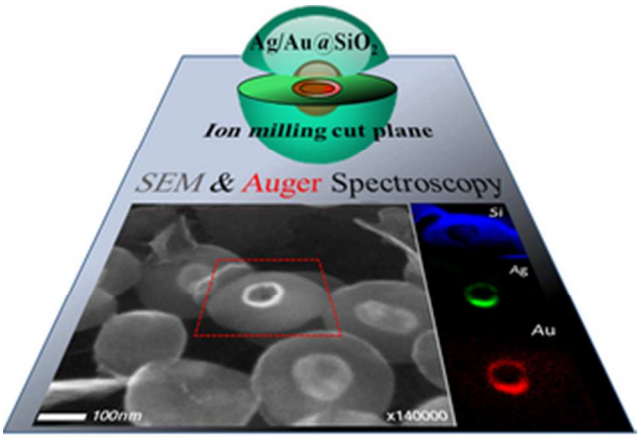

13x9mm (600 x 600 DPI)

Name	Position (eV)	FWHM (eV)	Atomic % Conc.
Au 4f 7/2	84.7	0.9	0.3
Au 4f 5/2	88.4	0.8	
Si 2p 3/2 (SiO_2)	103.6	1.6	22.2
Si 2p 1/2 (SiO_2)	104.2	1.6	
Ag 3d 5/2	368.6	1.1	0.2
Ag 3d 3/2	374.5	0.7	
O 1s (SiO_2)	532.9	1.5	33.6
O 1s (C-O-C)	534.6	2.3	
C 1s (CC-CH)	285.0	1.5	43.7
C 1s (C-O)	286.5	2.9	

Fig 1 :

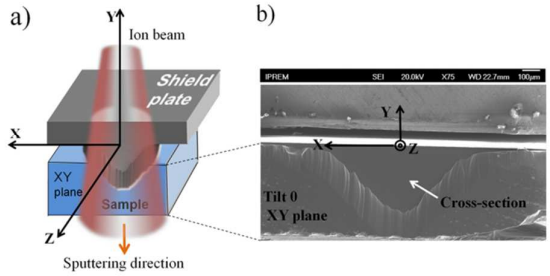

Fig 2 :

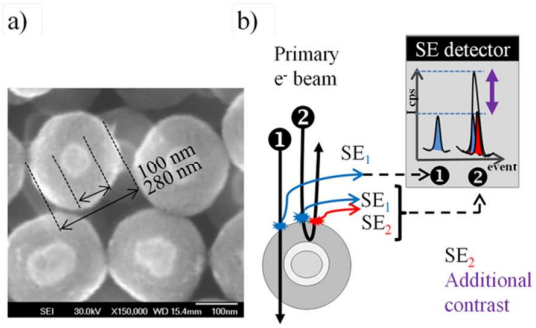

Fig 3 :

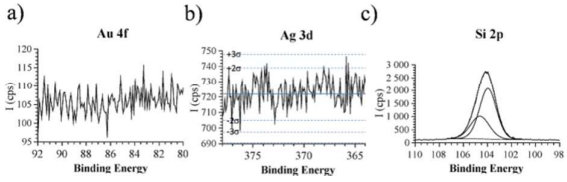

Fig 4 :

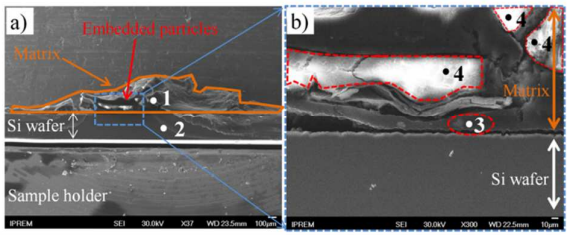

Fig 5 :

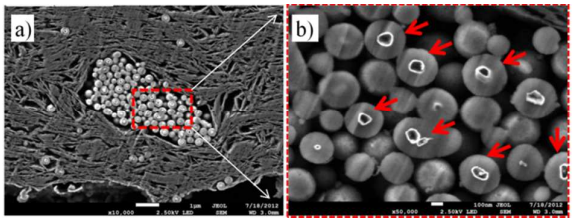

Fig 6 :

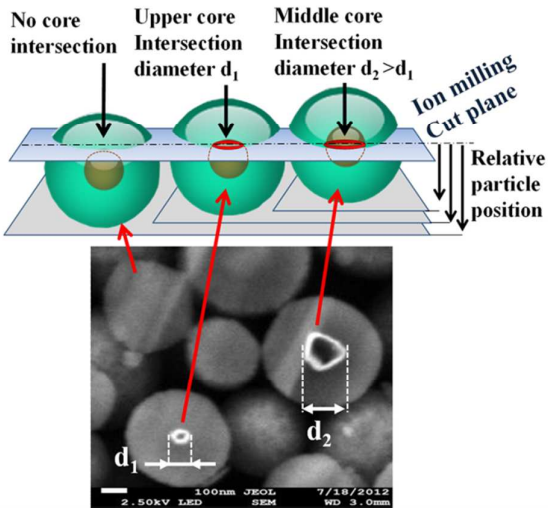

Fig 7 :

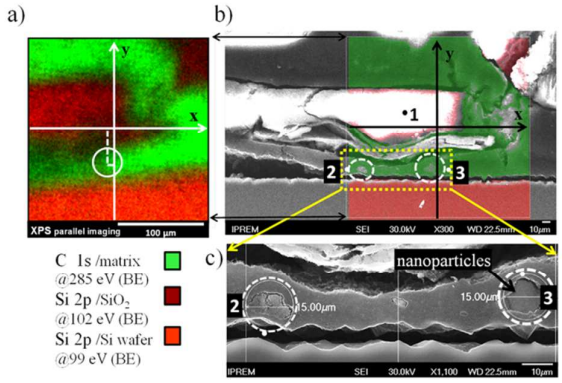

Fig 8 :

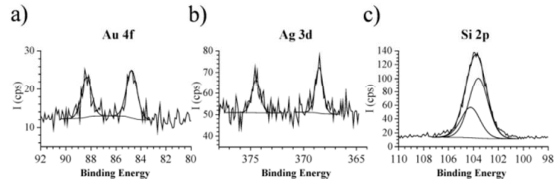

Fig 9 :

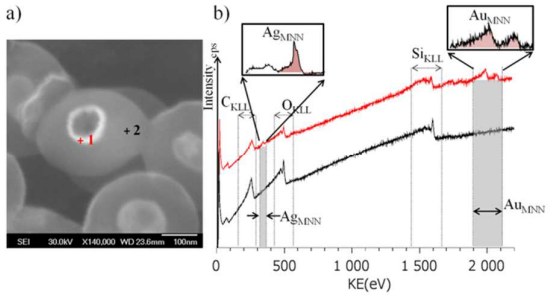

Fig 10 :

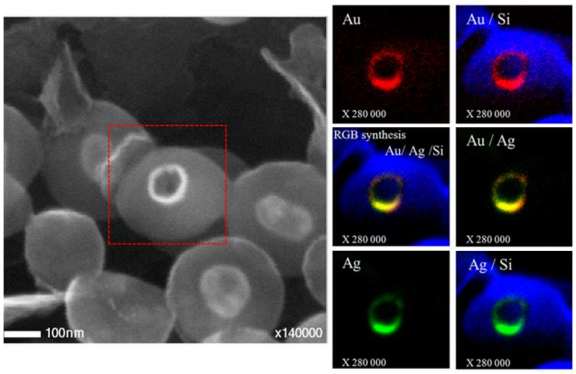

Fig 11 :

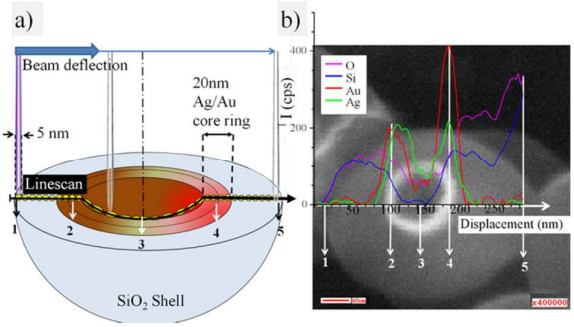

Fig 12 :

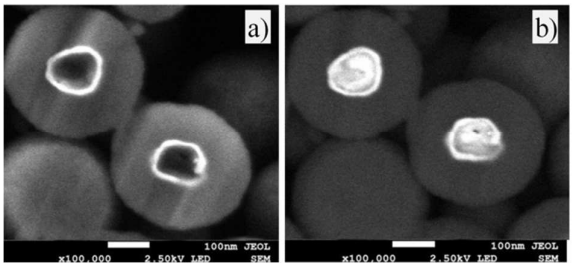

ESI 1:

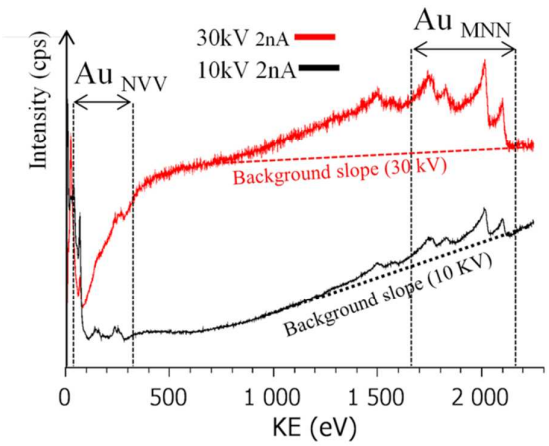

ESI2 :

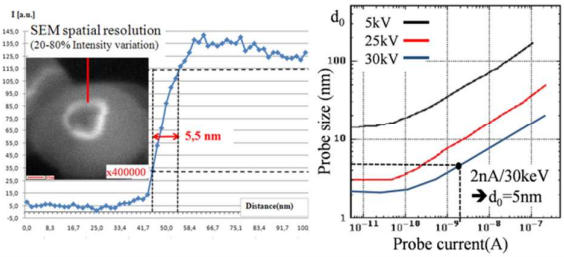

Graphical abstract: